Available online at www.sciencedirect.com
ScienceDirect
Trans. Nonferrous Met. Soc. China 34(2024) 1150−1166
Transactions of Nonferrous Metals Society of China
www.tnmsc.cn

Flash plasma electrolytic oxidation and electrochemical behaviour in physiological media of additive manufacturing Ti6Al4V alloy

H. MORA-SANCHEZ[1,2], C. RAMOS[1], M. MOHEDANO[1], B. TORRES[3], R. ARRABAL[1], E. MATYKINA[1]

1. Departamento de Ingeniería Química y de Materiales, Facultad de Ciencias Químicas, Universidad Complutense de Madrid, 28040 Madrid, Spain;
2. CIDETEC, Basque Research and Technology Alliance (BRTA), Po. Miramón 196, 20014 Donostia-San Sebastián, Spain;
3. Departamento Matemática Aplicada, Ciencia e Ingeniería de Materiales y Tecnología Electrónica, Universidad Rey Juan Carlos, C/Tulipán s/n, Móstoles 28933, Madrid, Spain

Received 1 November 2022; accepted 19 May 2023

Abstract: The objective of this work is to understand the plasma electrolytic oxidation (PEO) treatment and electrochemical behaviour of a Ti6Al4V alloy manufactured by a laser powder bed fusion additive manufacturing (AM) technique known as direct metal laser sintering (DMLS). Ca and P-containing coatings were produced with short time (<120 s) PEO treatments (also termed as Flash-PEO) obtaining 3−10 μm-thick coatings on both the AM alloy and a conventional counterpart. Subsequently, the electrochemical behaviour of the bare and treated alloys was assessed in a modified α-MEM solution via potentiodynamic polarization and electrochemical impedance spectroscopy (EIS). The fine α-lamellar microstructure of the AM alloy with small β-phase particles at the interlamellar spaces was seen to advance the onset of sparking promoting faster growth of PEO coating in comparison to the conventional alloy. Flash-PEO coatings enhanced the corrosion protection of both conventional and AM alloys, the thinnest (<3 μm) coatings providing up to three times greater protection. AM Ti6Al4V was found to be susceptible to localized crevice corrosion which could be assigned to the high grain boundary density. Flash-PEO treatments, even as short as 35 s, were sufficient to successfully prevent it.

Key words: additive manufacturing; laser powder bed fusion; plasma electrolytic oxidation; Flash-PEO; titanium; crevice corrosion; α-MEM

1 Introduction

Among the metallic systems used in the biomedical industry, commercially pure Ti and Ti6Al4V are the common choices for orthodontic and orthopaedic applications due to their good corrosion resistance in physiological media (i.e. highly stable TiO_2 passive layer), mechanical properties (i.e. elastic modulus ~100 GPa), and biocompatibiltity [1−5]. The fabrication of metallic implants has been revolutionized by additive manufacturing (AM) approaches which allow the cost-efficient and on-site production of dense near-net-shape 3D patient-customized implants from biomedical grade alloys [6−11]. Certainly, there has been a noticeable interest in the AM of Ti and its alloys, particularly in Ti6Al4V [12,13]. The most common metal AM technologies are those based on laser powder bed fusion (L-PBF). These technologies are based on the rapid melting and solidification of metallic powders in a layer-by-layer manner, using a high energy laser and following a 3D computer-aided design [9]. Ti and

Corresponding author: H. MORA-SANCHEZ, E-mail: hmora@cidetec.es
DOI: 10.1016/S1003-6326(23)66460-X

its alloys produced by L-PBF techniques present an as-built microstructure consisting of α' martensite as a result of the fast solidification taking place during the process. This microstructure is undesirable from the point of view of mechanical (i.e. low ductility) [14] and electrochemical (i.e. unstable in most media) [15,16] properties. For these reasons, L-PBF Ti6Al4V parts are generally subjected to sub-β transus annealing treatments (700−900 °C, 2−3 h) [17,18]. The electrochemical behaviour of AM Ti alloys in physiological media is generally considered similar or even superior to that of traditionally manufactured Ti6Al4V, although this is still under debate [16,19]. Susceptibility to localised corrosion of AM Ti alloys has been reported due to high surface roughness [20−22] and internal porosity [23−25].

With the aim to improve the osseointegration of Ti implants with the host bone, several surface modification techniques have been investigated: sand-blasting, chemical etching, anodizing, etc. [26,27]. Among the mentioned techniques, PEO treatment of Ti surfaces has already shown clinical success in immediate loading orthodontic procedures [28]. The PEO is an advanced high voltage anodizing technique that allows the fabrication of porous and rough ceramic coatings with the aid of short-lived plasma micro-discharges favouring the incorporation of bioactive elements (i.e. Ca, P, Zn and Mg) [29−33]. In comparison with traditional anodizing, PEO coatings improve the corrosion resistance and surface mechanical properties (i.e. hardness and adhesion). Moreover, the combination of surface topography, microstructure and composition of PEO coatings promote early cell-to-surface interactions [34]. In the last few years, with the aim to reduce treatment costs and minimize the impact on the mechanical properties of the substrate (i.e. fatigue), short PEO treatments (<120 s), termed as Flash-PEO, have been developed [35−37]. There is henceforth an increasing interest in studying PEO treatment of AM Ti6Al4V for biomedical applications [38−40]. The existing studies are focused on the use of aqueous suspensions for >5 min-long PEO treatments and their in vivo and in vitro bactericidal and osseointegration capacities. Moreover, there is a lack of knowledge on the effect of AM Ti6Al4V microstructures on the PEO process and the electrochemical behaviour of the resulting coatings in physiological media. Henceforth, the present work aims to develop Flash-PEO of an L-PBF Ti6Al4V alloy produced in a novel, transparent electrolyte and to study the electrochemical behaviour of the bare and PEO-treated alloy in an inorganic α-MEM medium.

2 Experimental

2.1 Base materials

The selected reference material was a hot-rolled mill-annealed Ti6Al4V sheet with a microstructure consisting of equiaxed α grains and smaller β aggregates (Figs. 1(a, b)). In the following, reference alloy specimens will be labelled as RA. The L-PBF manufacturing of the AM Ti6Al4V alloy was carried out by Fundación Idonial (Asturias, Spain) using a M280 EOS direct metal laser sintering system (EOS GmbH, Germany). The powder feedstock had a particle size in the 20−63 μm range. Dense 30 mm × 30 mm × 30 mm cubes were printed with the following parameters: laser power and spot size of 280 W and 0.07 mm, respectively; layer thickness of 0.03 mm; hatching spacing of 0.09 mm; and scanning speed of 1200 mm/s. The laser scanning strategy consisted of a default 5 mm "stripe hatching pattern" covering the whole printing area, as shown in Fig. 1(c). Alternating scans were performed by the laser along the entire length of the stripes. In order to minimize residual stresses, the scanning pattern was rotated by 67° for each subsequent layer. The as-built cubes were subjected to a stress-relief thermal treatment at 300 °C for 2 h followed by furnace cooling. In order to transform the as-built α' acicular microstructure into α lamella + β microstructure, an additional thermal treatment at 750 °C for 3.5 h followed by furnace cooling was applied to the cubes. The AM specimens were extracted in the *XY* direction (i.e. parallel to the building platform), as shown in Fig. 1(d), with dimensions of 30 mm × 10 mm × 3 mm. SEM micrographs demonstrated that the heat treated AM *XY* microstructure consisted of α lamella and small β aggregates at the grain boundaries (Figs. 1(e, f)).

2.2 Plasma electrolytic oxidation

Prior to the PEO treatment, the specimens were ground by successive SiC sandpapers down to P4000. Following grinding, the specimens were

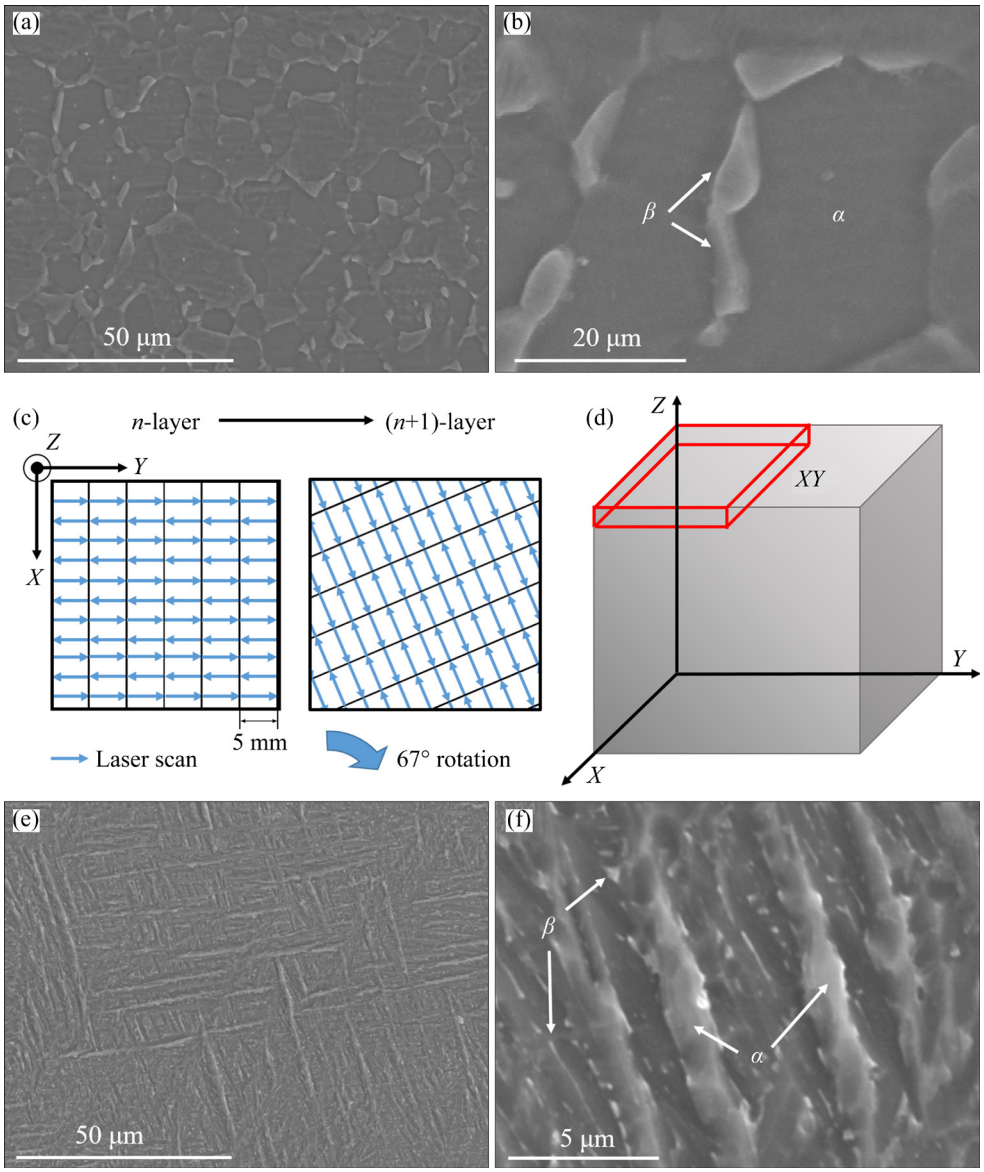

Fig. 1 SEM images of RA alloy (a, b); Scanning strategy during AM processing of Ti6Al4V alloy (c), Schematic diagram of AM specimens extraction in *XY* direction (d); SEM images of AM alloy (e, f)

chemically etched for 20−30 s in the following solution: 48 mL H_2O + 40 mL HNO_3 + 12 mL HF. The specimens were subsequently attached to a copper wire as electrical contact and electrically insulated with a commercial stopping-off resin (Lacquer 45, MacDermid plc), maintaining an unmasked 1 or 3 cm^2 working area (depending on the specimen size). The thickness of the coatings was measured right after the PEO process using an eddy-current meter (ISOSCOPE FMP10, Fischer), equipped with an FTA3.3H probe, taking an average of 10 measurements. Porosity was estimated by analysis of SEM images per specimen with an area of approximately 1100 μm^2 each using the ImageJ software for image processing and analysis. Images were converted to black and white binary images to allow pore identification. The particle analysis tool of the ImageJ software was used to calculate the population density, pore size and area. Most pores were rounded close to a circle. However, pores could also appear elongated, approximating an ellipse. Because of this, pore size reported herein corresponded to the largest dimension identified and it will be referred to as "diameter" due to the large population of rounded pores. The porosity is given as a percentage corresponding to the ratio of area covered by pores (sum of the areas of all the pores) divided by the total area of the image. Cross-section porosity was estimated in the same way.

The electrolyte was a Ca and P-containing aqueous solution with the following composition: 0.05 mol/L $C_6H_{10}CaO·5H_2O$, 0.055 mol/L $NaH_2PO_4·2H_2O$, 0.025 mol/L NaOH, and 0.15 mol/L $Na_2(EDTA)·2H_2O$. The PEO treatment was carried out with an AC square voltage signal with 490 V positive pulse and 30 V negative pulse (V_{RMS}=347 V) at 300 Hz and 50% duty cycle. The initial rise of the voltage was controlled by a 60 s ramp. The current density was limited to a maximum of 300 mA/cm^2.

The PEO specimens for the subsequent characterization and testing were fabricated on both alloys at 120 s (Long treatment, PEO-L: RA-L and AM-L) to ensure ~10 μm thick coatings and at 35 s (Short treatment, PEO-S: RA-S and AM-S) to obtain the thinnest coating possible in full sparking conditions. Additionally, to study any possible effect of the AM microstructure on the PEO treatment, in comparison with the RA microstructure, a set of coatings were fabricated at the onset of sparking, i.e. establishment of the PEO regime. During the 120 s treatments, the onset of sparking was identified as the first instant in which sparks were visible on the surface of the samples: 20−30 s.

2.3 Corrosion testing

2.3.1 Electrochemical tests (OCP, EIS and PDP)

The bare RA and AM specimens for corrosion testing followed the same preparation and electrical assembly specified for the PEO treatment. A modified α-MEM solution only containing inorganic compounds was selected as physiological medium: 6.8 g/L NaCl, 0.2 g/L $CaCl_2$, 0.098 g/L $MgSO_4$, 0.4 g/L KCl, 2.2 g/L $NaHCO_3$ and 0.122 g/L Na_2HPO_4 (diluted in distilled water, pH: 7.4−7.6). The electrochemical tests were carried out using a Gamry Interface1010E Potentiostat/Galzanostat/ZRA (Gamry Instruments, USA) and a Ag/AgCl as a reference electrode and graphite as a counter electrode. A double-wall cell connected to a water thermostat was used in order to maintain the electrolyte temperature at ~37 °C during the experiments. At least two specimens of each condition were tested in order to ensure repeatability. The following testing sequence was applied for each specimen: open circuit potential (OCP) → electrochemical impedance spectroscopy (EIS) → potentiodynamic polarization (PDP). The testing medium was maintained throughout the whole sequence. Specimens were immersed in the medium and the OCP was continuously measured for 1 h. The EIS tests were performed applying a sinusoidal 10 mV amplitude signal with respect to the measured OCP in the frequency range from 10^5 to 0.01 Hz. The impedance spectra were fitted with ZView software via equivalent electrical circuits maintaining chi-squared values below 0.01 to ensure the goodness of the fit. For each individual parameter of the equivalent circuits, the errors were kept below 5%. Polarization curves were recorded in the voltage range between −0.5 and 3.5 V with respect to the OCP with a scan rate of 0.5 mV/s.

2.3.2 Crevice corrosion tests

A secondary set of bare AM Ti specimens were prepared by covering the whole sample with the stopping-off resin and, upon curing, 1−3 cm^2 working area was unmasked by cutting through the resin with the help of a scalpel and peeling it off. The objective of this was to create a crevice between the resin and the material. The estimated height, width and depth of the crevice are below 1 mm. This is a common defect that might unintentionally appear during the laboratory experimentation. The samples were subsequently subjected to the same testing procedure detailed in Section 2.3.1.

3 Results and discussion

3.1 Onset of PEO

Figure 2(a) depicts the root mean square voltage (V_{RMS}, V) and current density (J_{RMS}, mA/cm^2) vs treatment time (s) during the PEO process for both RA and AM alloys for 120 s. The PEO treatment of both alloys showed a high degree of repeatability. During the first 20 s of the process (Fig. 2(b)), the V_{RMS} increased linearly while the J_{RMS} remained at a plateau of 50 mA/cm^2, indicating thickening of a barrier film. After 20 s, the J_{RMS} experimented a dramatic increase up to 300 mA/cm^2, where it remained until the end of the treatment. This was accompanied by visible sparking on the surface of the specimens and by slower increasing rate of the V_{RMS}. This indicated the dielectric breakdown of the growing anodic film, i.e. onset of sparking (OS), and the subsequent growth of new coating over the specimen by the action of microdischarges beyond 30 s.

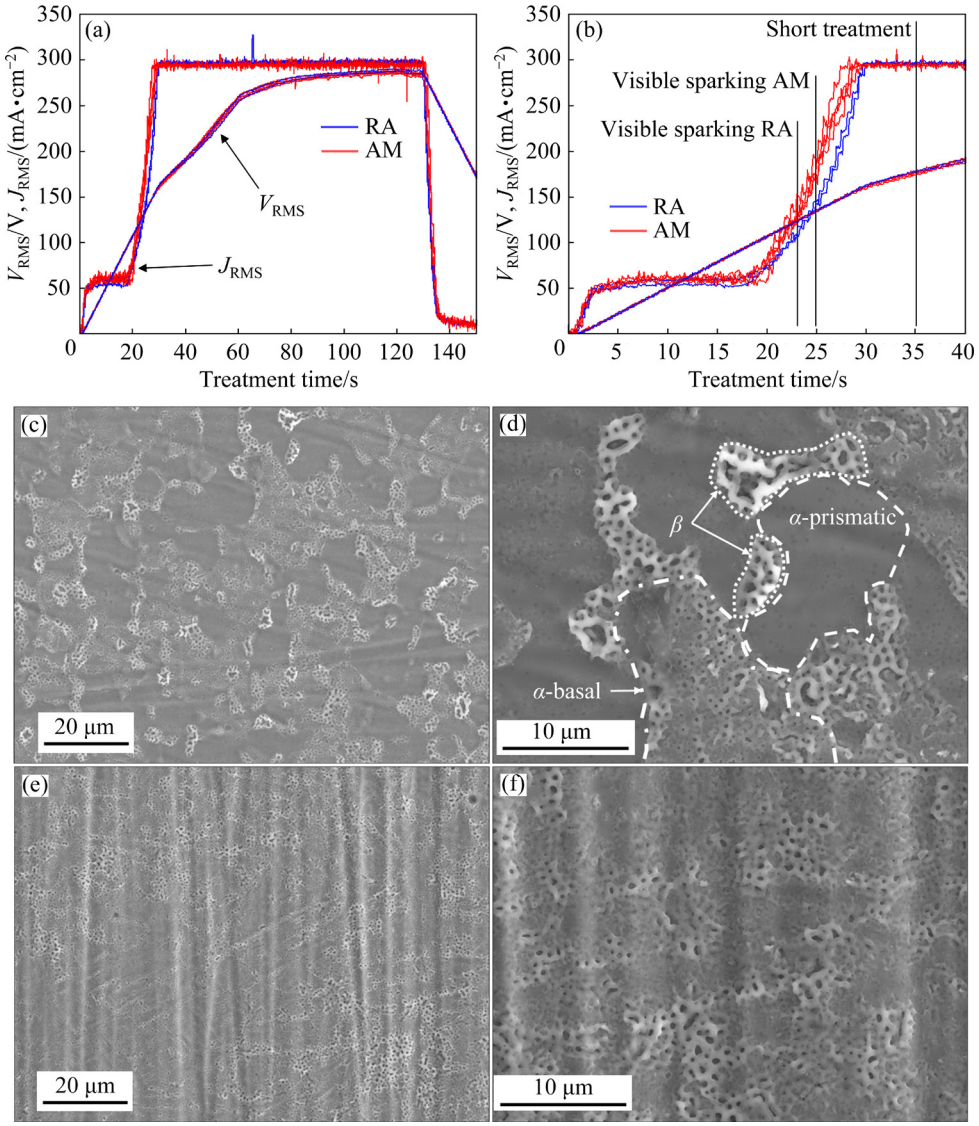

Fig. 2 V_{RMS} and J_{RMS} vs time curves during PEO treatments (a, b), SEM images of RA-OS coating (c, d); SEM images of AM-OS coating (e, f)

Visible sparks were observed at ~23 s on the RA alloy and at ~25 s on the AM alloy. Interestingly, the AM alloy experimented a faster J_{RMS} rise, which indicates a more conductive anodic film than that formed on the RA alloy during this stage (Fig. 2(b)). SEM images of the coatings fabricated at the onset of sparking on the RA and AM alloys are shown in Figs. 2(c, d) and Figs. 2(e, f), respectively. A trimodal surface morphology was found in the RA-OS specimen (Figs. 2(c, d)), which resembled the equiaxed $\alpha+\beta$ microstructure observed in Figs. 1(a, b): (1) rough regions with small pores enclosed by the boundaries of equiaxed α grains, which correspond to the growth of PEO coating, (2) regions with coarser PEO pores distributed in a chain-like fashion that, based on their size and shape, are likely to have formed over β grains, and (3) smoother equiaxed areas that correspond to pre-PEO anodic film in which darker spots are observed.

These spots might be related to O_2 bubbles or dielectric breakdown within the film. This suggested that the dielectric breakdown of the growing anodic film and subsequent sparking depended on the crystallographic phase and orientation. It is well known that TiO_2 film growth is accompanied by O_2 evolution as a result of the amorphous-to-crystalline transformation of the film [41,42]. This results in entrapment of O_2 bubbles within the anodic film which ultimately leads to rupture of the film [43]. Defects in the anodic film are considered preferential discharge

sites. MATYKINA and co-workers [44] investigated the dependence of O_2 evolution on the crystallographic orientation of pure Ti during anodizing in potassium phosphate solutions at pre-sparking voltages. They found that the O_2 evolution rate was higher in basal-oriented (with respect to specimen surface) grains than in prismatic-oriented grains. Henceforth, it can be concluded that the difference between the morphologies (1) and (3) corresponds to the difference in crystallographic orientation.

The AM-OS specimen presented a homogeneously rough surface with numerous pores (Fig. 2(e)). Images at higher magnification (Fig. 2(f)) showed that most of the surface corresponds to PEO coating, although partially ruptured pre-PEO anodic film without pores is also observed. The distribution of the pores appeared to follow the lamellar pattern of the AM alloy, possibly due to preferential breakdown over the β-phase (Fig. 2(f)). It is worth recalling the large grain boundary density and predominant presence of α-phase in the AM alloy microstructure. Grain boundaries tend to induce defects in the growing titania anodic film. Such defects subsequently become preferential sites for O_2 evolution and, ultimately, microdischarges. Therefore, the large grain boundary density and the small finely distributed β-phase of AM specimen randomize the location of microdischarges, minimizing the chances of repetitive breakdown at the same location, thus resulting in smaller pores.

It can be concluded then that PEO coating growth is more uniform in the AM specimen due to the greater population density of β-phase particles and larger grain boundary area associated with the lamellar α-phase. On the other hand, in the RA specimen, initial coating growth occurs preferentially over the β-phase and basal α-phase grains.

3.2 PEO coating growth after onset of sparking

Figures 3(a) and 3(b) depict the surface morphology of the RA-S and AM-S coatings, respectively, formed up to 35 s treatment. The RA alloy still shows localized growth of PEO coating material, indicating that higher voltages are required to induce microdischarges at the prismatic α grains (Fig. 3(a)). On the other hand, the AM specimen shows a uniform PEO coating (Fig. 3(b)). This is again attributed to the fine dispersion of β-phase particles and grain boundary density in the AM alloy acting as preferential locations for dielectric breakdown. The slightly higher thickness and surface roughness (S_a) values, presented in

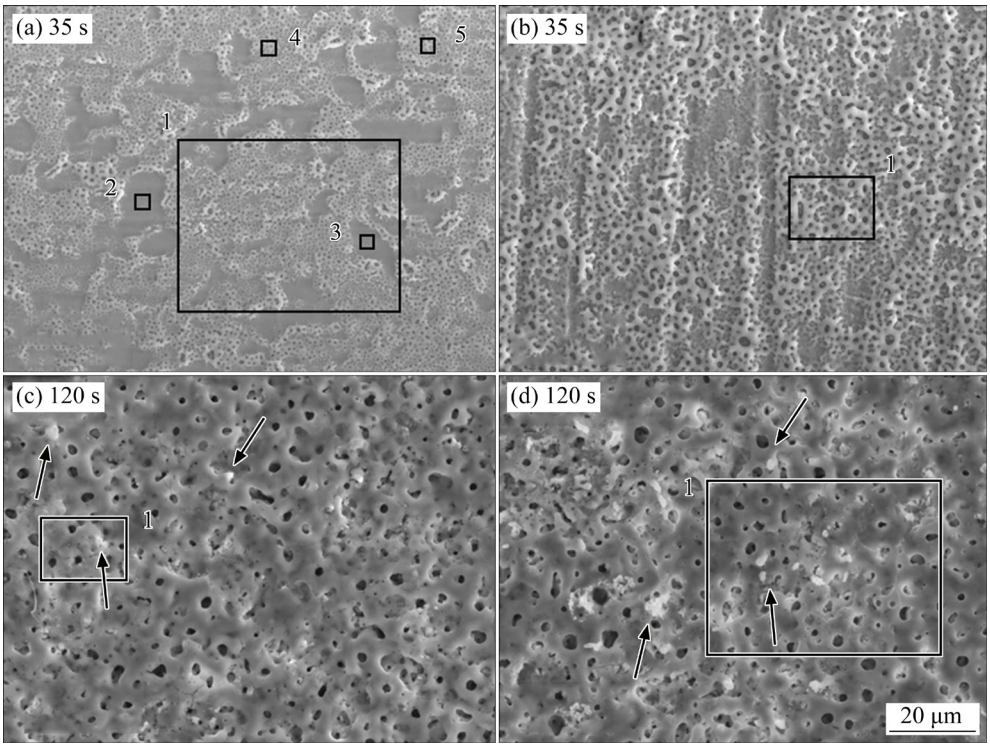

Fig. 3 Surface SEM images of RA-S (a), AM-S (b), RA-L (c) and AM-L (d) coatings (Numbered squares mark the areas analysed by EDS)

Table 1, are consistent with a more homogeneous (i.e. advanced) PEO regime in the AM-S specimen, which is clearly evidenced in Fig. 3(b).

Moreover, as given in Table 2, pores were larger for the AM alloy which is in line with the higher J_{RMS} values during the initial stages of PEO (note that only the PEO-like areas were used to calculate porosity values for the RA-S specimen).

Plan views of the RA-L and AM-L coatings (120 s) are shown in Figs. 3(c) and 3(d), respectively. There were not significant differences between the RA-L and AM-L coatings except for a slightly larger thickness and pore size in the AM-L coating (Tables 1 and 2).

As expected, the longer treatment time produced thicker coatings and bigger pores due to the increasing intensity of the microdischarges. The mean and maximum pore size increased with the treatment time while the pore population decreased, in agreement with stronger discharges at longer treatment time. Interestingly, this led to a slightly lower net surface porosity most likely related to the significant decrease in pore population.

Cross-sectional examination of the coatings formed in 35 s shows a clear effect of the substrate microstructure (Fig. 4). The AM alloy (Figs. 4(c, d)) features a more porous barrier layer and a uniform outer layer with bigger pores. On the other hand, the coating morphology on the RA alloy (Figs. 4(a, b)) is largely influenced by the massive β-phase particles and the basal α-grains. Preferential

Table 1 Thickness and surface roughness (S_a) of RA-PEO and AM-PEO specimens

Specimen	Thickness/μm	S_a/μm
RA-S	2.2±0.4	0.2±0.02
AM-S	2.7±0.9	0.3±0.04
RA-L	11±0.6	0.7±0.1
AM-L	12±0.9	0.7±0.03

Table 2 Pore data estimated from image analysis of SEM images (Fig. 3)

Specimen	Population/10^{-3} μm^{-2}	Mean size/μm	Max size/μm	Porosity/%	CS porosity/%
RA-S	738±103	0.5±0.3	2.7	9	–
AM-S	314±5	0.8±0.6	4.8	11	–
RA-L	71±6	1±0.7	7.4	6	19±0.1
AM-L	78±22	1.1±0.8	9.3	6	24±0.1

CS porosity: Percentage of area covered by porosity within the cross-section of the coatings

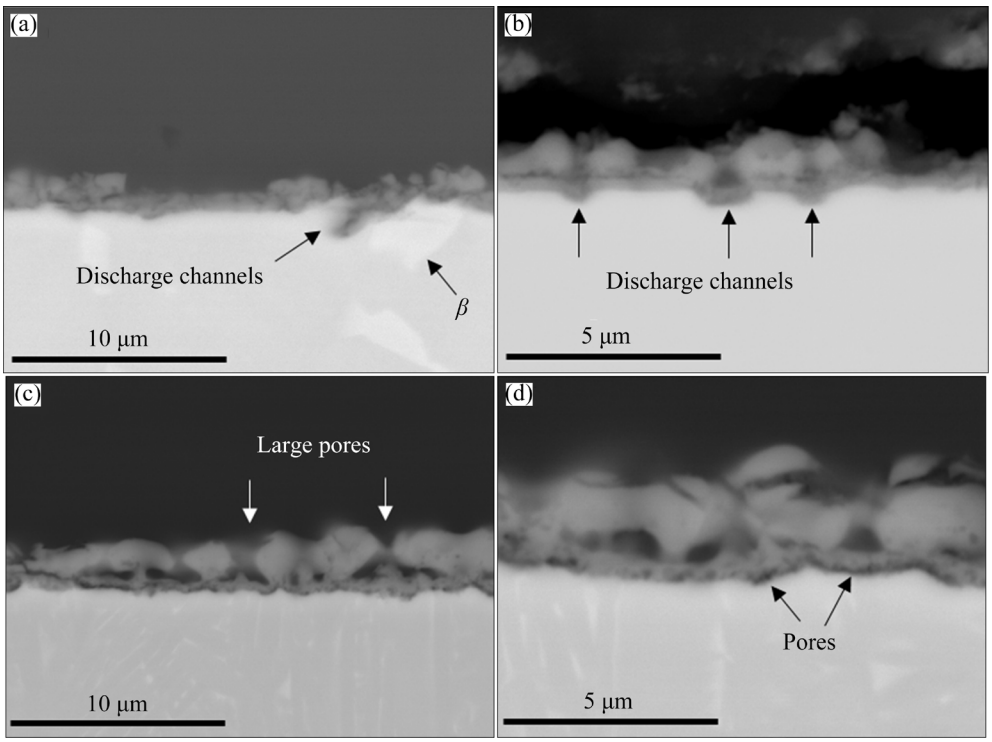

Fig. 4 Cross-sectional SEM images of RA-S (a, b) and AM-S (c, d) coatings formed in 35 s

dielectric breakdown occurs in the vicinity of the β-phase, leading to thickening of the outer PEO layer, whereas the thinner coating regions show a less defective, or more uniform film, which is possibly formed over the basal α-grains.

After 120 s of the treatment, the coating morphology on both alloys becomes largely similar. They consist of an outer porous region, which accounts ~80% of the coating thickness, and a barrier layer (~1 μm) with enclosed fine nanometric pores (Fig. 5). The most significant difference was the slightly larger porosity in the outer coating layer for AM-L (24% vs 19%, Table 2). Several pore morphologies are observed: (1) vertical large pores, possibly corresponding to discharge channels associated with strong Type B discharges [45], (2) random-shape cavities close to the inner layer, which might correspond to secondary internal Types D and E discharges [46], and (3) rounded micro- and nano-pores related to O_2 evolution and gas entrapment. Thermal cracks were also found across the compact material of this layer.

3.3 Elemental and phase composition of PEO coatings

The chemical composition of the coatings given in Table 3 was measured by means of EDS. Locations of the EDS measurements are indicated in Figs. 3(a−d). In addition to O and Ti due to the formation of TiO_2, EDS revealed the incorporation of electrolyte-derived elements (i.e. Na, P and Ca) as well as Al and V from the substrate. Regarding the short treatments, the AM-S specimen showed higher levels of Ca and P with respect to the conventional counterpart, possibly due to more intense microdischarges promoting the incorporation of electrolyte elements. The same effect is observed when comparing prismatic and basal α grains in RA-S specimens: higher amounts of Ca and P are found in locations with more developed PEO morphology (i.e. basal grains).

Coatings formed in 120 s presented similar compositions, Ca and P being slightly higher in the AM-L specimen. Plan view surface analyses revealed a much higher amount of Ca in these specimens when compared with shorter treatment time (~8 at.% vs 1−2 at.% Ca).

Figure 6 depicts the cross-sections of the RA-L and AM-L specimens and the corresponding P and Ca distribution in EDS maps. It is evident that the inner coating material is enriched in P (7−10 at.% P, Figs. 6(c, d), Table 3). The Ca/P ratios clearly show the preferential distribution of Ca and P in the outer and inner regions of the coatings, respectively.

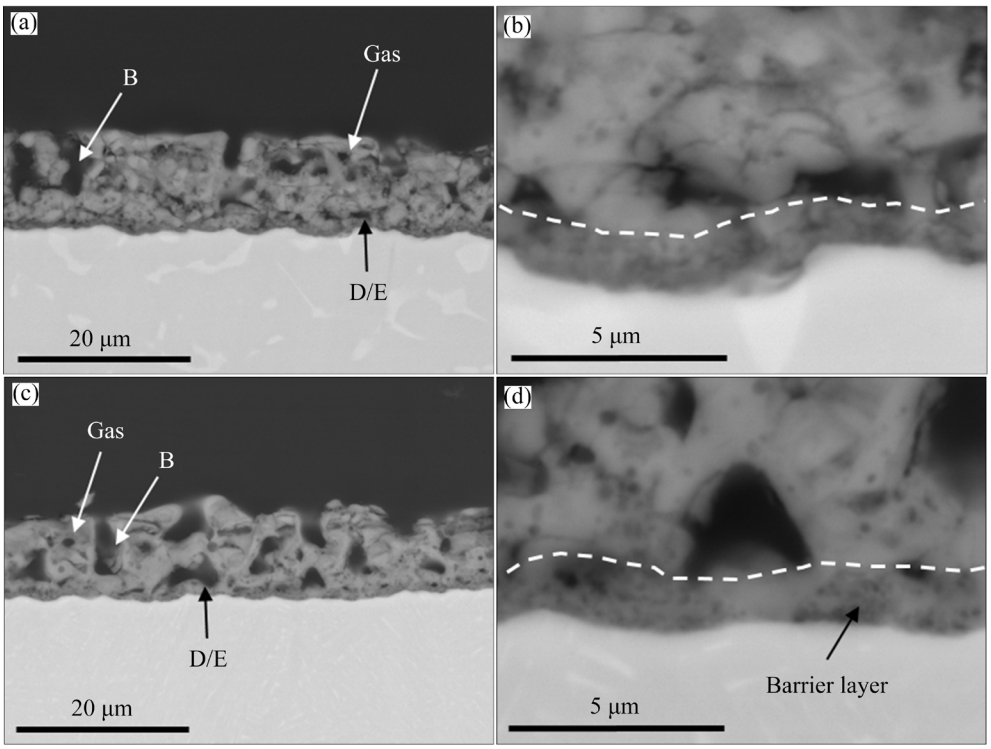

Fig. 5 Cross-sectional SEM images of RA-L (a, b) and AM-L (c, d) coatings formed in 120 s (Dashed line indicating the barrier layer; Type B, D and E discharges and porosity arising from O_2 evolution and gas entrapment are indicated)

Table 3 Elemental composition measured by EDS for locations shown in Figs. 3 and 6

Specimen	Location	Content/at.%							Ca/P
		O	Na	Al	P	Ca	Ti	V	
RA-S	1 (Plan view)	69	0.5	2.7	1.5	0.9	28	1	0.6
	2 (Prismatic α)	66	0.3	3.2	0.4	0.1	30	0.7	0.4
	3 (Prismatic α)	63	−	2.6	0.9	0.5	31	1.9	0.5
	4 (Basal α)	63	0.3	2.8	1.3	0.7	30	1.1	0.5
	5 (Basal α)	66	0.5	2.7	1.7	1.1	27	1.2	0.6
AM-S	1 (Plan view)	68	0.4	2	4.6	2.2	22	0.7	0.5
RA-L	1 (Plan view)	69	0.7	1.2	7.1	8.3	13	0.4	1.2
	2 (Inner layer)	73	1	2	7.4	1.3	15	0.4	0.2
	3 (Outer layer)	62	0.1	1.6	1.9	1.3	33	0.6	0.7
AM-L	1 (Plan view)	68	0.9	1.2	7.2	8.8	13	0.4	1.2
	2 (Inner layer)	64	0.3	2.6	10.4	1.9	20	0.9	0.2
	3 (Puter layer)	70	0.1	1.6	2.3	1.7	23	0.7	0.7

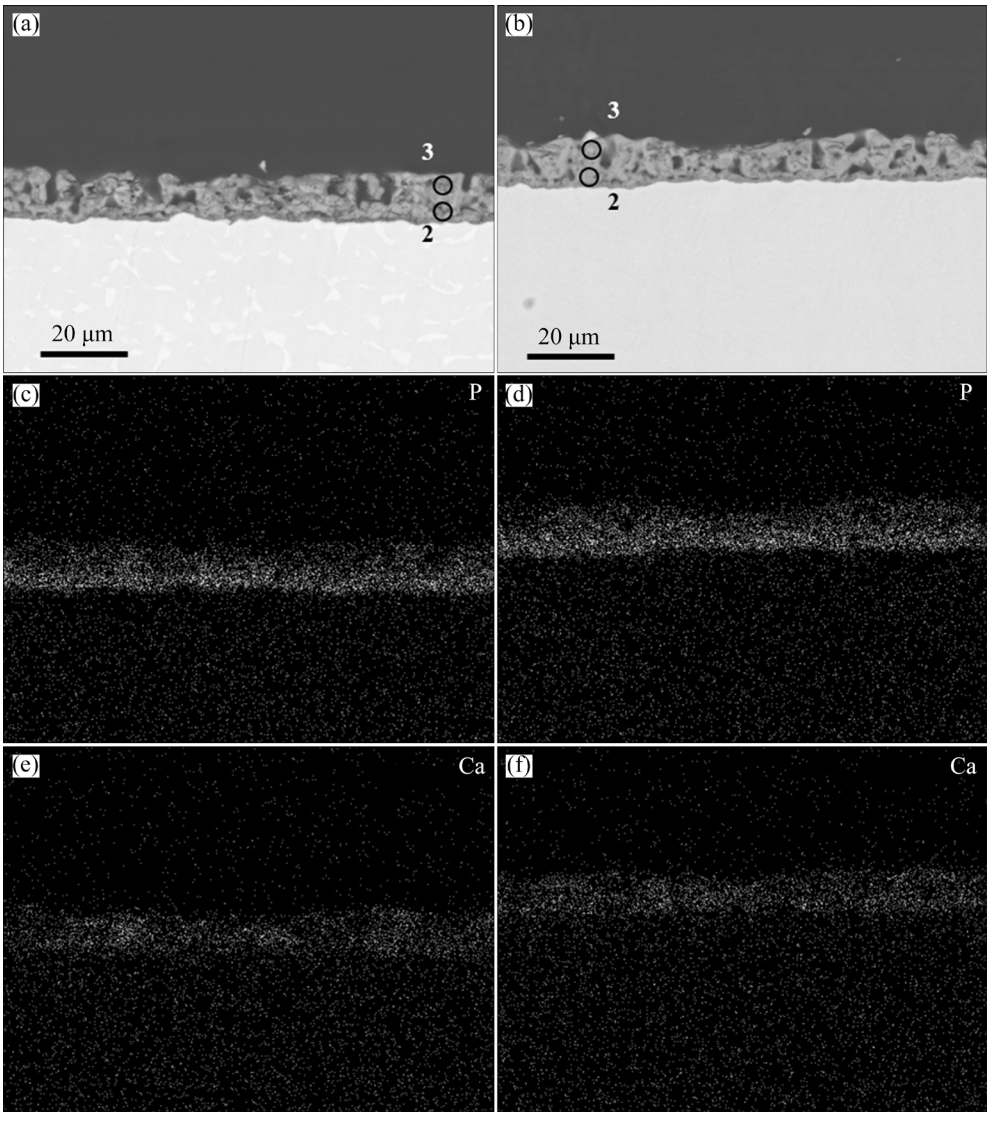

Fig. 6 EDS P and Ca elemental maps of cross-sections of RA-L (a, c, e) and AM-L (b, d, f) coatings

This is a common observation for phosphate-containing electrolytes and is related to the inwards migration of phosphate ions during PEO [47,48]. Ca appears to be more homogeneously distributed without visible enrichment at the surface (Figs. 6(e, f)). Considering the high Ca levels found by EDS (plan views), it is inferred that Ca-rich regions on the surface correspond to relatively loose and discrete precipitates, as is often the case for Ca−P-based coatings on Ti [49], that are easily detached during preparation of cross-section specimens. The locations of these precipitates are marked in Figs. 3(c, d) with arrows.

Diffraction patterns from the RA-S and AM-S revealed diffractions from the Ti substrate, particularly the Ti hcp α phase [50] (Fig. 7). In the case of the RA-S specimen, a weak peak appeared at 39.3° corresponding to the Ti bcc β phase. For AM-S, a diffraction in the vicinity of 40.44° Ti-α diffraction corresponded to β phase transformed from ternary and quartic α' martensite [51,52]. Specimens RA-L and AM-L presented the characteristic peaks of TiO_2 anatase and rutile phases, identified by the ICDD cards 00-004-0477 and 00-021-1276, respectively. These oxide diffractions were absent or weak in the RA-S and AM-S specimens, indicating that crystallization of the amorphous oxide did not take place for such short treatments. Diffractions corresponding to $Ca_3(PO_4)_2$ (ICDD card 00-009-0348) were found in the RA-L and AM-L coatings in agreement with the evidence of Ca and P presence in EDS. Nevertheless, the weak contribution of this phase indicates that it is mostly present within the coatings as amorphous material. Amorphous calcium phosphate is known to crystallize at 600−800 °C into α-tricalcium phosphate (α-TCP) [53], which is at the same time a precursor for the formation of hydroxyapatite (HA, $Ca_5(PO_4)_3OH$) [54]. HA has been already reported for PEO coatings on Ti6Al4V produced with the same treatment as in the present work for treatment time above 300 s [55].

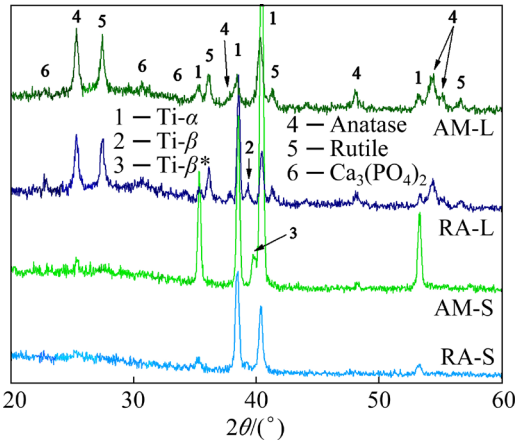

Fig. 7 XRD patterns of RA-S, AM-S, RA-L and AM-L coatings

3.4 Corrosion characterization

3.4.1 Open circuit potential and potentiodynamic polarization

The open circuit potential (OCP) and potentiodynamic polarization (PDP) curves of the bare and PEO treated specimens are shown in Figs. 8(a, b), respectively. OCP values and electrochemical parameters obtained from the PDP curves, such as corrosion and passivation potentials (φ_{corr} and φ_{pass}) and corrosion and passivation current densities (J_{corr} and J_{pass}), are gathered in Table 4. Both RA and AM alloys showed negative OCP while the PEO treated samples had positive

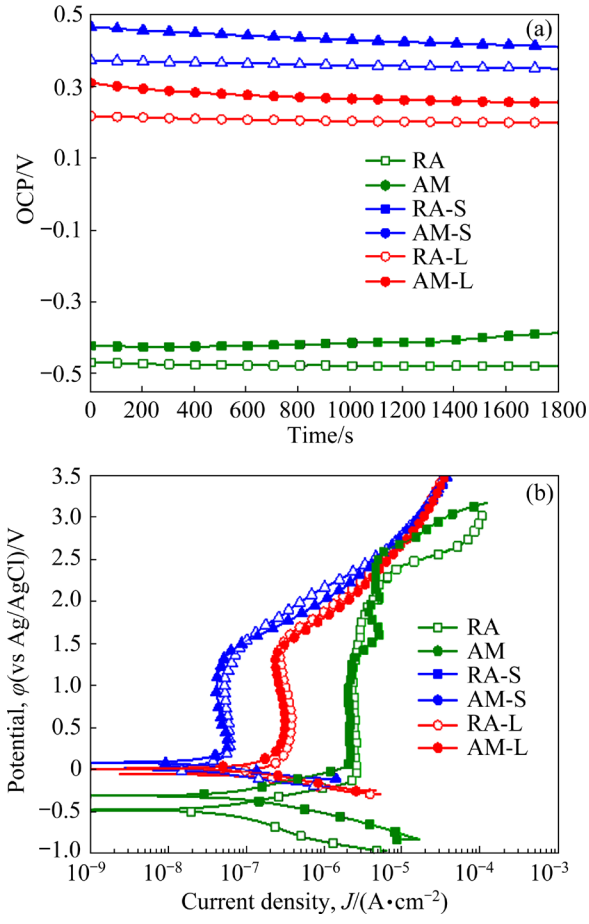

Fig. 8 Electrochemical characterization of bare alloys and PEO-treated specimens: (a) Open circuit potential (OCP); (b) Potentiodynamic polarization (PDP)

Table 4 Electrochemical data gathered from tests shown in Fig. 8

Specimen	OCP/ V	φ_{corr}/ V	J_{corr}/ (A·cm^{-2})	φ_{pass}/ V	J_{pass}/ (A·cm^{-2})	φ_O/ V
RA	−0.48	−0.48	5.6×10^{-8}	−0.1	2.5×10^{-6}	2
AM	−0.32	−0.32	1.1×10^{-7}	0.1	2.5×10^{-6}	1.3
RA-S	0.35	0.01	2.2×10^{-8}	0.2	5.6×10^{-8}	1.5
AM-S	0.41	0.08	2.2×10^{-8}	0.2	4.7×10^{-8}	1.5
RA-L	0.20	−0.06	1×10^{-7}	0.2	3.4×10^{-7}	1.5
AM-L	0.26	0.01	9.3×10^{-8}	0.3	2.9×10^{-7}	1.4

values. This is a common observation for PEO coated materials due to improved passivity of the surface [56,57]. The shift of the OCP between bare alloys and PEO-treated ones is of the order of 1 V, which is higher than that previously reported in the literature [49,58].

φ_{corr} values of the bare alloys were very similar to the OCP values. However, the PEO-treated specimens had corrosion potentials near 0 V. That is to say, they became more active as a result of polarization. This shift is commonly observed for titanium and is related to the charging process of the electrode/solution interface capacitance. Despite the relatively slow scan rate used in this study (0.5 mV/s), which is a well-known strategy for minimizing this artefact [59], PEO treated specimens, unlike the bare substrates, showed sufficiently high charging current to shift φ_{corr} to significantly lower values than OCP.

The J_{corr} values of studied specimens were in the range of 10^{-8} A/cm^2 (Table 4). This is in agreement with the excellent corrosion resistance of titanium in neutral chloride containing media. All the specimens showed an anodic branch with a distinct passive region, although clear differences were observed among the three surface conditions. The bare substrates revealed the highest passive current densities (~2.5×10^{-6} A/cm^2). The PEO-coated specimens showed smaller values due to the formation of a thicker barrier layer. Surprisingly, the RA-S and AM-S specimens showed lower values (~5×10^{-8} A/cm^2) than the RA-L and AM-L specimens (~3×10^{-7} A/cm^2). This suggests that, after 120 s, the barrier layer has more crystalline and defects (nanoporosity) due to gas entrapment [47]. Note that, as evidenced by XRD, both RA-L and AM-L show anatase and rutile. On the other hand, this might also suggest that the larger pore size and the porosity of the outer layer in the 120 s coatings allowed the permeation of the electrolyte while this was prevented in the 35 s coatings due to the finer porosity.

For all specimens, the passive range was followed by the increase of the current density due to O_2 evolution above the potential for water oxidation, further referred to as φ_O. The bare alloys revealed higher φ_O values (>2 V) than the PEO-treated specimens (~1.5 V). This could be explained by the higher passive currents in the bare alloys resulting in their intersection with the water oxidation reaction at higher potentials. Another relevant feature in Fig. 8(b) is that the cathodic branch on PEO-treated specimens is shifted to much higher current densities in comparison to the bare alloys. This is attributed to the crystallinity of the PEO coating material which is more conductive than the amorphous passive film on the substrates, thus facilitating the oxygen reduction reaction.

Polarization curves of PEO-coated specimens do not show relevant differences between AM and RA materials. However, in regards to bare alloys, it is interesting to note that the φ_O value of the AM specimen is ~0.25 V higher than that of RA, which is almost equal to the shift observed in the cathodic branch. Considering that TiO_2 is an n-type semi-conductor, this behaviour would be consistent with a higher charge carrier density in the passive film of the AM material shifting the flatband potential towards the conduction band, thus facilitating oxygen reduction and increasing the overpotential for water oxidation [60].

3.4.2 Electrochemical impedance spectroscopy

Complex, Nyquist and Bode plots obtained from EIS are presented in Figures 9(a, b, c), respectively. Each set of specimens presented well differentiated responses: (1) bare substrates revealed a predominantly capacitive behaviour, typical of Ti alloys, (2) RA-S and AM-S presented two time constants at high and low frequency ranges and a diffusion response at intermediate frequencies, and (3) RA-L and AM-L presented three time constants, two at high frequency and one at low frequencies. According to this, three different equivalent circuits were used to fit the EIS spectra. Bare substrates were fitted with a two element circuit (Fig. 9(d)) including the contributions from space charge (CPE_{sc}/R_{sc}) and barrier properties of the passive film (CPE_b/R_b). The best fit for the

RA-S and AM-S specimens was found with an equivalent circuit consisting of a finite open circuit diffusion W_o element and a CPE_b/R_b element, both nested inside a CPE_{ocl}/R_{ocl} element (Fig. 9(e)) corresponding to the response of the outer compact layer (OCL). Finally, the RA-L and AM-L specimens were fitted with a three-element circuit accounting for the contributions from the OCL, space charge and barrier layer (Fig. 9(f)). The fitting data for the three set of samples are presented in Tables 5−7. In all cases, the electrolyte resistance, R_e, was 20−30 Ω·cm^2.

The AM substrate presented a slightly higher total impedance than the RA substrate at 0.01 Hz. The lower CPE_{sc} and CPE_b as well as the higher R_{sc} and R_b values are indicative of a thicker passive film for the AM specimen with a wider space charge region within it (Table 5).

RA-S and AM-S specimens presented nearly identical total impedance at 0.01 Hz (Table 6). The obtained values were significantly higher (~370 kΩ·cm^2) than those of the bare substrates (~175 kΩ·cm^2) and long treatments (~130 kΩ·cm^2), in agreement with the PDP experiments. The fitting results indicated a higher R_b and lower R_{ocl} and W_O-R for the AM-S than for the RA-S specimens. This is in agreement with the larger pore size (Table 1) and a somewhat thicker barrier layer formed in AM-S since, as shown in SEM micrographs, PEO developed more uniformly in this specimen.

3.4.3 Crevice corrosion

Figure 10(a) compares polarization behaviour of duplicates corresponding to the bare AM substrate with and without crevice corrosion (the specimens with crevice corrosion were prepared according to the procedure explained in Section 2.3.2). It can be seen that the specimens that suffered crevice corrosion presented a dramatic increase of the current density above 10^{-5} A/cm^2 at

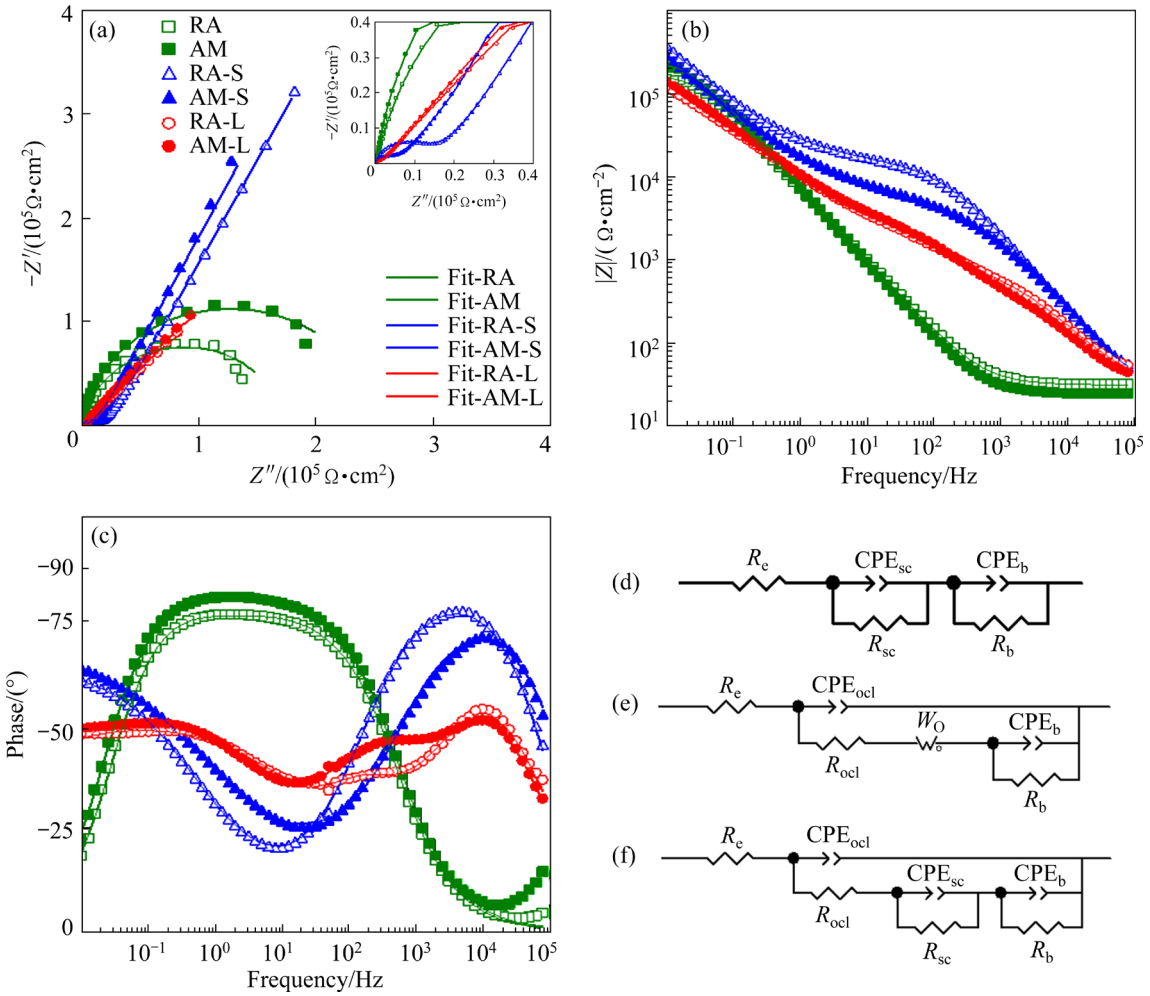

Fig. 9 Complex (a), Nyquist (b) and Bode (c) plots obtained from EIS and equivalent circuits used to fit EIS data (d−f): (d) Bare RA and AM substrates; (e) PEO treated specimens at 35 s; (f) PEO treated specimens at 120 s

Table 5 Fitted equivalent electric circuit parameters for EIS spectra of substrates

Specimen	$\|Z\|_{0.01Hz}$/(kΩ·cm^2)	CPE_{sc}/(μS·s^n·cm^{-2})	n	R_{sc}/(kΩ·cm^2)	CPE_b/(μS·s$^{n'}$·cm^{-2})	n'	R_b/(kΩ·cm^2)
RA	144	198	0.72	1.6	28	0.93	171
AM	207	115	0.73	417	30	0.95	558

Table 6 Fitted equivalent electric circuit parameters for EIS spectra of short PEO treated specimens

Specimen	$\|Z\|_{0.01Hz}$/(kΩ·cm^2)	CPE_{ocl}/(μS·s^n·cm^{-2})	n	R_{ocl}/(kΩ·cm^2)	W_O-T/s	n'	W_O-R/(kΩ·cm^2)	CPE_b/(μS·s$^{n''}$·cm^{-2})	n''	R_b/(kΩ·cm^2)
RA-S	370	0.2	0.92	10.1	0.4	0.35	24	101	0.90	3
AM-S	371	0.3	0.88	2.8	0.2	0.36	18	37	0.79	10

Table 7 Fitted equivalent electric circuit parameters for EIS spectra of long PEO treated specimens

Specimen	$\|Z\|_{0.01Hz}$ /(kΩ·cm^2)	CPE_{ocl}/(μS·s^n·cm^{-2})	n	R_{ocl}/(kΩ·cm^2)	CPE_{sc}/(μS·s$^{n'}$·cm^{-2})	n'	R_{sc}/(kΩ·cm^2)	CPE_b/(μS·s$^{n''}$·cm^{-2})	n''	R_b/(kΩ·cm^2)
RA-L	121	0.9	0.80	0.7	5.9	0.85	0.7	36	0.57	1339
AM-L	141	0.9	0.82	0.5	6.1	0.72	1.7	34	0.60	1160

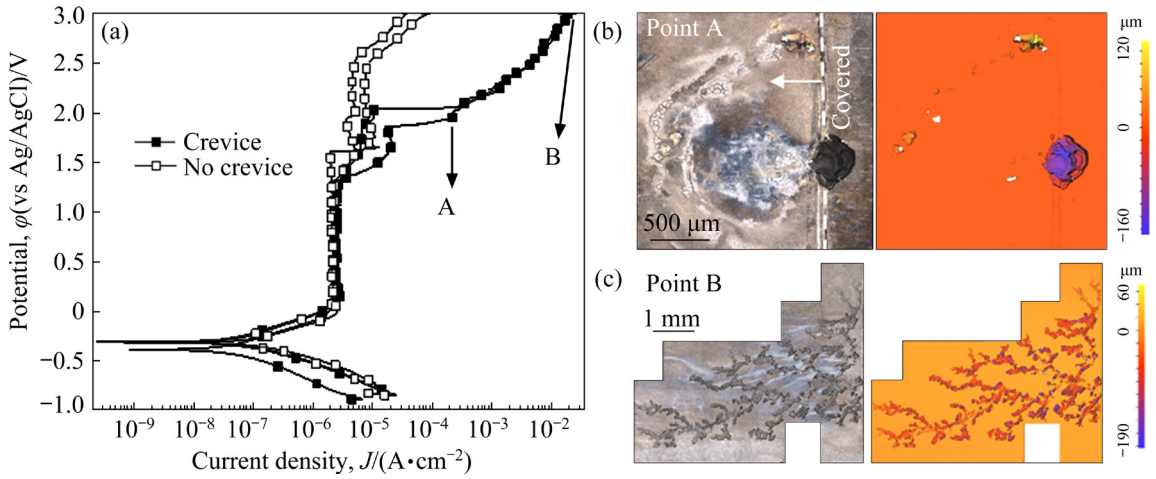

Fig. 10 PDP curves of bare AM samples showing normal behaviour and crevice corrosion (a); Optical 3D measurements of localized corrosion at Point A in (a) (Testing area was to the left of the dashed line as indicated by the arrow) (b); Optical 3D measurements of specimen at Point B in (a) showing extended corrosion over surface (c)

the potentials above ~1.5 V. As shown in Fig. 10(b), localised corrosion initiated in the vicinity and beneath the insulating resin (Point A in Fig. 10(a)). By the end of the PDP tests (Point B in Fig. 10(a)), corrosion with a filiform-like appearance greatly extended to the rest of the working surface (Fig. 10(c)). Crevice corrosion was accompanied by the formation of a loosely adherent light-brown gel on the surface. This gel is a typical product of Ti^{4+} hydrolysis that occurs at pH above 4 and contains Ti hydroxides ($Ti(OH)_x^{(4-x)}$) among other products [61]. This is consistent with other crevice corrosion studies on Ti [62,63].

Within the restricted volume of the crevice, dissolved O_2 and other oxidizing species are consumed faster than they can be replenished from the bulk solution, inducing a microelectrochemical cell where the crevice becomes the anode and the exposed surface is the cathode. The solution within the crevice reaches low pH levels with the hydrolysis of titanium chlorides that form hydrochloric acid and Ti hydroxide, inducing rapid localized active corrosion [63]. DAMBORENEA and co-workers [61] showed localised crevice corrosion of DMLS Ti6Al4V pins at superficial porosity and imperfections. They also reported the

formation of white $TiO_2 \cdot H_2O$, which is more soluble than TiO_2. Dissolution of this oxide can produce TiO_2^{2+}, which subsequently precipitates as $TiO_3 \cdot H_2O$. These oxides present higher solubility and worse adherence than TiO_2, henceforth offering a worse corrosion protection. The formation of these oxides is in agreement with the light-brown gel observed in the present work. It can be hypothesized that the Ti hydroxides and hydrated oxide were formed at the early stages within the crevice (Fig. 10(b)) and later extended over the surface creating additional crevices under the gel, which drove the corrosion attack much like a filiform undercoating corrosion (Fig. 10(c)).

It is remarkable that neither the bare RA specimen nor any of PEO-treated alloys presented this behaviour. In comparison with RA, AM alloy presents a significantly higher number of grain boundaries which favours ion migration [64]. Grain boundaries act as oxide formation sites [65] which may lead to defects in the passive film upon coalescence of growing oxide. Defects or grain boundaries within the passive film represent ion migration pathways [64]. The shift of the φ_O and cathodic branch observed in the polarization curves suggested a higher charge carrier density within the passive film of the AM alloy compared to the RA. HE et al [66] argued that dissolution pathways along grain boundaries might lead to cation hydrolysis and subsequent lowering of the pH within the crevice. Since O_2 is depleted at the crevice and the occluded regions, Ti ions cannot form a new film and dissolve into the medium, while Cl^- ions proceed to the dissolution of the film [67]. Higher grain boundary density might explain the susceptibility of AM alloy to localized crevice corrosion, in comparison to the RA alloy. These findings are concerning given the growing significance of AM Ti alloys and risk of unintentional crevices in prosthesis assemblies. Further studies regarding localised crevice corrosion of AM Ti alloys are henceforth required.

4 Conclusions

(1) Additive manufacturing of Ti6Al4V by L-PBF produces a fine α-lamellar microstructure with small β-phase particles at the interlamellar spaces that promotes an earlier onset dielectric breakdown and faster development of PEO coating growth. This differs from PEO processing of the conventional Ti6Al4V alloy, which is largely affected by the massive β-phase particles and α grain orientation.

(2) PEO coatings improve the corrosion resistance of the Ti6Al4V alloy in inorganic α-MEM. Thin coatings resulting from short treatments (35 s) present better corrosion behaviour than thicker coatings (120 s) possibly due to the formation of a less defective barrier layer with lower crystallinity.

(3) The bare AM alloy is susceptible to crevice corrosion during polarization, which can be associated with its larger grain boundary area facilitating Ti dissolution within the crevice. Such behaviour is not observed for the conventional alloy. Findings also revealed that a thin PEO coating on the AM alloy is sufficient to avoid crevice corrosion under the studied conditions.

CRediT authorship contribution statement

H. MORA-SANCHEZ: Conceptualization, Methodology, Validation, Formal analysis, Investigation, Writing – Original draft, Writing – Review & editing, Visualization, Supervision; **C. RAMOS:** Formal analysis, Investigation, Writing – Original draft, Visualization; **M. MOHEDANO:** Supervision, Writing – Review & editing, Resources, Project administration, Funding acquisition; **B. TORRES:** Writing – Review & editing, Resources, Funding acquisition; **R. ARRABAL:** Conceptualization, Supervision, Writing – Review & editing, Resources, Project administration, Funding acquisition; **E. MATYKINA:** Conceptualization, Supervision, Validation, Formal analysis, Writing – Review & editing, Resources, Project administration, Funding acquisition.

Declaration of competing interest

The authors declare that they have no known competing financial interests or personal relationships that could have appeared to influence the work reported in this paper.

Acknowledgments

The authors gratefully acknowledge the support of PID2021-124341OB-C22 and PID2021-124341OB-C21 (MCIU/AEI/FEDER, UE) and ADITIMAT-CM (S2018/NMT-4411, Regional Government of Madrid and EU Structural Funds). M. MOHEDANO is grateful for the support of RYC-2017-21843. H. MORA-SANCHEZ is

grateful for the support of PEJD-2019-POST/IND-16119 (Regional Government of Madrid and EU Structural Funds) and FEI-EU-20-05 (UCM).

References

[1] CHEN Q, THOUAS G A. Metallic implant biomaterials [J]. Materials Science and Engineering R: Reports, 2015, 87: 1−57.

[2] GEETHA M, SINGH A K, ASOKAMANI R, GOGIA A K. Ti based biomaterials, the ultimate choice for orthopaedic implants—A review [J]. Progress in Materials Science, 2009, 54: 397−425.

[3] GOTMAN I. Characteristics of metals used in implants [J]. Journal of Endourology, 1997, 11: 383−389.

[4] LONG M, RACK H. Titanium alloys in total joint replacement — A materials science perspective [J]. Biomaterials, 1998, 19: 1621−1639.

[5] RACK H J, QAZI J I. Titanium alloys for biomedical applications [J]. Materials Science and Engineering C, 2006, 26: 1269−1277.

[6] GU D D, MEINERS W, WISSENBACH K, POPRAWE R. Laser additive manufacturing of metallic components: Materials, processes and mechanisms [J]. International Materials Reviews, 2012, 57: 133−164.

[7] HERZOG D, SEYDA V, WYCISK E, EMMELMANN C. Additive manufacturing of metals [J]. Acta Materialia, 2016, 117: 371−392.

[8] DEBROY T, WEI H, ZUBACK J, MUKHERJEE T, ELMER J, MILEWSKI J, BEESE A M, WILSON-HEID A D, DE A, ZHANG W. Additive manufacturing of metallic components–Process, structure and properties [J]. Progress in Materials Science, 2018, 92: 112−224.

[9] LIU S Y, SHIN Y C. Additive manufacturing of Ti6Al4V alloy: A review [J]. Materials & Design, 2019, 164: 23.

[10] LIU T Y, MIN X H, ZHANG S, WANG C S, CHUANG D. Microstructures and mechanical properties of Ti−Al−V−Nb alloys with cluster formula manufactured by laser additive manufacturing [J]. Transactions of Nonferrous Metals Society of China, 2021, 31: 3012−3023.

[11] QIANG L, HUANG Q, LI J J, HE Q F, NAKAI M, ZHANG K, NIINOMI M, YAMANAKA K, CHIBA A, NAKANO T. Microstructure and mechanical properties of Ti−Nb−Fe−Zr alloys with high strength and low elastic modulus [J]. Transactions of Nonferrous Metals Society of China, 2022, 32: 503−512.

[12] YAN R Z, LUO D M, HUANG H T, LI R X, YU N, LIU C K, HU M, RONG Q G. Electron beam melting in the fabrication of three-dimensional mesh titanium mandibular prosthesis scaffold [J]. Scientific Reports, 2018, 8: 1−10.

[13] CHO H R, ROH T S, SHIM K W, KIM Y O, LEW D H, YUN I S. Skull reconstruction with custom made three-dimensional titanium implant [J]. Archives of Craniofacial Surgery, 2015, 16: 11.

[14] MIERZEJEWSKA Z A, HUDAK R, SIDUN J. Mechanical properties and microstructure of DMLS Ti6Al4V alloy dedicated to biomedical applications [J]. Materials, 2019: 12: 176.

[15] DAI N A W, ZHANG L C, ZHANG J X, ZHANG X, NI Q Z, CHEN Y, WU M L, YANG C. Distinction in corrosion resistance of selective laser melted Ti−6Al−4V alloy on different planes [J]. Corrosion Science, 2016, 111: 703−710.

[16] SANDER G, TAN J, BALAN P, GHARBI O, FEENSTRA D R, SINGER L, THOMAS S, KELLY R G, SCULLY J R, BIRBILIS N. Corrosion of additively manufactured alloys: A review [J]. Corrosion, 2018, 74: 1318−1350.

[17] YANG J J, YU H C, YIN J, GAO M, WANG Z M, ZENG X Y. Formation and control of martensite in Ti−6Al−4V alloy produced by selective laser melting [J]. Materials & Design, 2016, 108: 308−318.

[18] KASPEROVICH G, HAUSMANN J. Improvement of fatigue resistance and ductility of TiAl6V4 processed by selective laser melting [J]. Journal of Materials Processing Technology, 2015, 220: 202−214.

[19] SEO D I, LEE J B. Influence of heat treatment parameters on the corrosion resistance of additively manufactured Ti−6Al−4V alloy [J]. Journal of the Electrochemical Society, 2020, 167: 101509.

[20] CECCHEL S, FERRARIO D, CORNACCHIA G, GELFI M. Development of heat treatments for selective laser melting Ti6Al4V alloy: Effect on microstructure, mechanical properties, and corrosion resistance [J]. Advanced Engineering Materials, 2020, 22: 2000359.

[21] ACQUESTA A, MONETTA T. As-built EBM and DMLS Ti−6Al−4V parts: Topography–corrosion resistance relationship in a simulated body fluid [J]. Metals, 2020, 10: 1015.

[22] FOJT J, HYBÁŠEK V, KAČENKA Z, PRŮCHOVÁ E. Influence of surface finishing on corrosion behaviour of 3D printed TiAlV alloy [J]. Metals, 2020, 10: 1547.

[23] CHEN L Y, HUANG J C, LIN C H, PAN C T, CHEN S Y, YANG T L, LIN D Y, LIN H K, JANG J S C. Anisotropic response of Ti−6Al−4V alloy fabricated by 3D printing selective laser melting [J]. Materials Science and Engineering A, 2017, 682: 389−395.

[24] QIAN C, XU H, ZHONG Q. The influence of process parameters on corrosion behavior of Ti6Al4V alloy processed by selective laser melting [J]. Journal of Laser Applications, 2020, 32: 032010.

[25] CHIU T M, MAHMOUDI M, DAI W, ELWANY A, LIANG H, CASTANEDA H. Corrosion assessment of Ti−6Al−4V fabricated using laser powder-bed fusion additive manufacturing [J]. Electrochimica Acta, 2018, 279: 143−151.

[26] NOURI A, WEN C. Introduction to surface coating and modification for metallic biomaterials [C]//Surface Coating and Modification of Metallic Biomaterials. Chicago, 2015: 3−60.

[27] ASRI R I M, HARUN W S W, SAMYKANO M, LAH N A C, GHANI S A C, TARLOCHAN F, RAZA M R. Corrosion and surface modification on biocompatible metals: A review [J]. Materials Science and Engineering C, 2017, 77: 1261−1274.

[28] ALBREKTSSON T, WENNERBERG A. On osseo-integration in relation to implant surfaces [J]. Clinical Implant Dentistry and Related Research, 2019, 21: 4−7.

[29] RAFIEERAD A R, ASHRA M R, MAHMOODIAN R, BUSHROA A R. Surface characterization and corrosion behavior of calcium phosphate-base composite layer on titanium and its alloys via plasma electrolytic oxidation: A review paper [J]. Materials Science and Engineering C, 2015, 57: 397−413.

[30] YU J M, CHOE H C. Morphology changes and bone formation on PEO-treated Ti−6Al−4V alloy in electrolyte containing Ca, P, Sr, and Si ions [J]. Applied Surface Science, 2019, 477: 121−130.

[31] LIM S G, CHOE H C. Corrosion phenomena of PEO-treated films formed in solution containing Mn, Mg, and Si ions [J]. Applied Surface Science, 2019, 477: 50−59.

[32] HWANG I J, CHOE H C. Effects of Zn and Si ions on the corrosion behaviors of PEO-treated Ti−6Al−4V alloy [J]. Applied Surface Science, 2019, 477: 79−90.

[33] ZHAI D J, FENG K Q. Preparation of micro/nano-structured ceramic coatings on Ti6Al4V alloy by plasma electrolytic oxidation process [J]. Transactions of Nonferrous Metals Society of China, 2019, 29: 2546−2555.

[34] SANTOS-COQUILLAT A, MOHEDANO M, MARTINEZ-CAMPOS E, ARRABAL R, PARDO A, MATYKINA E. Bioactive multi-elemental PEO-coatings on titanium for dental implant applications [J]. Materials Science and Engineering C, 2019, 97: 738−752.

[35] DEL OLMO R, MOHEDANO M, VISSER P, MATYKINA E, ARRABAL R. Flash-PEO coatings loaded with corrosion inhibitors on AA2024 [J]. Surface and Coatings Technology, 2020, 402: 126317.

[36] WIERZBICKA E, VAGHEFINAZARI B, LAMAKA S V, ZHELUDKEVICH M L, MOHEDANO M, MORENO L, VISSER P, RODRÍGUEZ A, VELASCO J, ARRABAL R. Flash-PEO as an alternative to chromate conversion coatings for corrosion protection of Mg alloy [J]. Corrosion Science, 2021, 180: 109189.

[37] WIERZBICKA E, MOHEDANO M, MATYKINA E, ARRABAL R. Design and multidimensional screening of flash-PEO coatings for Mg in comparison to commercial chromium(VI) conversion coating [J]. Metals, 2021, 11: 337.

[38] VAN HENGEL I A, RIOOL M, FRATILA-APACHITEI L E, WITTE-BOUMA J, FARRELL E, ZADPOOR A A, ZAAT S A, APACHITEI I. Selective laser melting porous metallic implants with immobilized silver nanoparticles kill and prevent biofilm formation by methicillin-resistant *Staphylococcus aureus* [J]. Biomaterials, 2017, 140: 1−15.

[39] van HENGEL I A J, PUTRA N E, TIEROLF M, MINNEBOO M, FLUIT A C, FRATILA-APACHITEI L E, APACHITEI I, ZADPOOR A A. Biofunctionalization of selective laser melted porous titanium using silver and zinc nanoparticles to prevent infections by antibiotic-resistant bacteria [J]. Acta Biomaterialia, 2020, 107: 325−337.

[40] RAZZI F, FRATILA-APACHITEI L E, FAHY N, BASTIAANSEN-JENNISKENS Y M, APACHITEI I, FARRELL E, ZADPOOR A A. Immunomodulation of surface biofunctionalized 3D printed porous titanium implants [J]. Biomedical Materials, 2020, 15: 15.

[41] ALADJEM A. Anodic oxidation of titanium and its alloys [J]. Journal of Materials Science, 1973, 8: 688−704.

[42] YAHALOM J, ZAHAVI J. Electrolytic breakdown crystallization of anodic oxide films on A1, Ta and Ti [J]. Electrochimica Acta, 1970, 15: 1429−1435.

[43] HABAZAKI H, UOZUMI M, KONNO H, SHIMIZU K, SKELDON P, THOMPSON G E. Crystallization of anodic titania on titanium and its alloys [J]. Corrosion Science, 2003, 45: 2063−2073.

[44] MATYKINA E, ARRABAL R, SKELDON P, THOMPSON G E, HABAZAKI H. Influence of grain orientation on oxygen generation in anodic titania [J]. Thin Solid Films, 2008, 516: 2296−2305.

[45] HUSSEIN R O, NIE X, NORTHWOOD D O, YEROKHIN A, MATTHEWS A. Spectroscopic study of electrolytic plasma and discharging behaviour during the plasma electrolytic oxidation (PEO) process [J]. Journal of Physics D: Applied Physics, 2010: 43: 10.

[46] CHENG Y L, XUE Z G, WANG Q, WU X Q, MATYKINA E, SKELDON P, THOMPSON G E. New findings on properties of plasma electrolytic oxidation coatings from study of an Al−Cu−Li alloy [J]. Electrochimica Acta, 2013, 107: 358−378.

[47] MATYKINA E, ARRABAL R, SKELDON P, THOMPSON G E. Transmission electron microscopy of coatings formed by plasma electrolytic oxidation of titanium [J]. Acta Biomater, 2009, 5: 1356−1366.

[48] HABAZAKI H, SHIMIZU K, NAGATA S, SKELDON P, THOMPSON G, WOOD G. Ionic transport in amorphous anodic titania stabilised by incorporation of silicon species [J]. Corrosion Science, 2002, 44: 1047−1055.

[49] MOHEDANO M, GUZMAN R, ARRABAL R, LÓPEZ LACOMBA J L, MATYKINA E. Bioactive plasma electrolytic oxidation coatings—The role of the composition, microstructure, and electrochemical stability [J]. Journal of Biomedical Materials Research Part B: Applied Biomaterials, 2013, 101: 1524−1537.

[50] AHMADI S M, JAIN R, ZADPOOR A A, AYAS C, POPOVICH V A. Effects of heat treatment on microstructure and mechanical behaviour of additive manufactured porous Ti6Al4V [C]//3rd International Conference on Smart Material Research. Molbourne, Australia, 2017.

[51] TER HAAR G M, BECKER T H. Selective laser melting produced Ti−6Al−4V: Post-process heat treatments to achieve superior tensile properties [J]. Materials, 2018: 11: 146.

[52] ZHANG X Y, FANG G, LEEFLANG S, BOTTGER A J, ZADPOOR A A, ZHOU J. Effect of subtransus heat treatment on the microstructure and mechanical properties of additively manufactured Ti−6Al−4V alloy [J]. Journal of Alloys and Compounds, 2018, 735: 1562−1575.

[53] SOMRANI S, REY C, JEMAL M. Thermal evolution of amorphous tricalcium phosphate [J]. Journal of Materials Chemistry, 2003, 13: 888−892.

[54] CARRODEGUAS R G, de AZA S. Alpha-tricalcium phosphate: Synthesis, properties and biomedical applications [J]. Acta Biomater, 2011, 7: 3536−3546.

[55] SANTOS-COQUILLAT A, GONZALEZ TENORIO R, MOHEDANO M, MARTINEZ-CAMPOS E, ARRABAL R, MATYKINA E. Tailoring of antibacterial and osteogenic properties of Ti6Al4V by plasma electrolytic oxidation [J]. Applied Surface Science, 2018, 454: 157−172.

[56] FAZEL M, SALIMIJAZI H, SHAMANIAN M, APACHITEI I, ZADPOOR A. Influence of hydrothermal treatment on the surface characteristics and electrochemical behavior of Ti−6Al−4V bio-functionalized through plasma electrolytic oxidation [J]. Surface and Coatings Technology, 2019, 374: 222−231.
[57] CHENG Y L, WU X Q, XUE Z G, MATYKINA E, SKELDON P, THOMPSON G. Microstructure, corrosion and wear performance of plasma electrolytic oxidation coatings formed on Ti−6Al−4V alloy in silicate-hexametaphosphate electrolyte [J]. Surface and Coatings Technology, 2013, 217: 129−139.
[58] MATYKINA E, ARRABAL R, MOHEDANO M, PARDO A, MERINO M C, RIVERO E. Stability of plasma electrolytic oxidation coating on titanium in artificial saliva [J]. J Mater Sci Mater Med, 2013, 24: 37−51.
[59] ZHANG X, JIANG Z H, YAO Z P, SONG Y, WU Z D. Effects of scan rate on the potentiodynamic polarization curve obtained to determine the Tafel slopes and corrosion current density [J]. Corrosion science, 2009, 51: 581−587.
[60] NOEL J. The electrochemistry of titanium corrosion [D]. 1999.
[61] de DAMBORENEA J J, ARENAS M A, LAROSA M A, JARDINI A L, ZAVAGLIA C A D, CONDE A. Corrosion of Ti6Al4V pins produced by direct metal laser sintering [J]. Applied Surface Science, 2017, 393: 340−347.
[62] PARIONA M, MÜLLER I. An electrochemical study of the crevice corrosion of titanium [J]. Journal of the Brazilian Chemical Society, 1997, 8: 137−142.
[63] BHOLA R, BHOLA S M, MISHRA B, OLSON D L. Corrosion in titanium dental implants/prostheses—A review [J]. Trends Biomater Artif Organs, 2011, 25: 34−46.
[64] NELSON J, ORIANI R. Stress generation during anodic oxidation of titanium and aluminum [J]. Corrosion Science, 1993, 34: 307−326.
[65] RALSTON K, BIRBILIS N. Effect of grain size on corrosion: A review [J]. Corrosion, 2010, 66: 7500501−7500513.
[66] HE X, NOËL J J, SHOESMITH D W. Temperature dependence of crevice corrosion initiation on titanium grade-2 [J]. Journal of the Electrochemical Society, 2002, 149: B440.
[67] LI J, LIN X, WANG J, ZHENG M, GUO P, ZHANG Y, REN Y, LIU J, HUANG W. Effect of stress-relief annealing on anodic dissolution behaviour of additive manufactured Ti−6Al−4V via laser solid forming [J]. Corrosion Science, 2019, 153: 314−326.

增材制造 Ti6Al4V 合金的闪速等离子体电解氧化与在生理介质中的电化学行为

H. MORA-SANCHEZ[1,2], C. RAMOS[1], M. MOHEDANO[1], B. TORRES[3], R. ARRABAL[1], E. MATYKINA[1]

1. Departamento de Ingeniería Química y de Materiales, Facultad de Ciencias Químicas, Universidad Complutense de Madrid, 28040 Madrid, Spain;
2. CIDETEC, Basque Research and Technology Alliance (BRTA), Po. Miramón 196, 20014 Donostia-San Sebastián, Spain;
3. Departamento Matemática Aplicada, Ciencia e Ingeniería de Materiales y Tecnología Electrónica, Universidad Rey Juan Carlos, C/Tulipán s/n, Móstoles 28933, Madrid, Spain

摘　要：研究激光粉末床熔融增材制造(AM)(又称直接金属激光烧结)技术制备的 Ti6Al4V 合金等离子体电解氧化(PEO)处理及其电化学行为。通过短时间(<120 s)PEO 处理(也称闪速 PEO)，在 AM 合金和传统合金表面制备了 3~10 μm 厚、含 Ca 和 P 的涂层。然后在改良的 α-MEM 溶液中，通过动电位极化曲线和电化学阻抗谱(EIS)评估了合金的电化学行为。与传统合金相比，AM 合金中形成了细小的层片状 α 显微组织和层间小尺寸的 β 相颗粒，这促使了火花的产生，从而促进了 PEO 涂层的生长。闪速 PEO 涂层提高了传统合金和 AM 合金的耐腐蚀性，最薄的涂层(<3 μm)提供了高达 3 倍的保护。AM Ti6Al4V 由于其高的晶界密度，易受局部缝隙腐蚀的影响。而即使短至 35 s 的闪速 PEO 处理也足以成功避免这种情况。

关键词：增材制造；激光粉末床熔融；等离子体电解氧化；闪速 PEO；钛；缝隙腐蚀；α-MEM

(Edited by Bing YANG)